Article

Dependence of thermal infrared emissive behaviors of snow cover on the surface snow type

Masahiro Hori[1*], Teruo Aoki[2], Tomonori Tanikawa[1], Katsuyuki Kuchiki[2], Masashi Niwano[2], Satoru Yamaguchi[3] and Sumito Matoba[4]

[1] Earth Observation Research Center, Japan Aerospace Exploration Agency, 2-1-1, Sengen, Tsukuba, Ibaraki 305-8505, Japan

[2] Meteorological Research Institute, 1-1 Nagamine, Tsukuba, Ibaraki 305-0052, Japan

[3] Institute of Low Temperature Science, Hokkaido University, Nishi 8, Kita 19, Sapporo, 060-0819 Japan

[4] Snow and Ice Research Center, National Research Institute for Earth Science and Disaster Prevention, Suyoshi-machi, Nagaoka 940-0821, Japan

* *Corresponding author* E-mail address: hori.masahiro@jaxa.jp

Keywords: brightness temperature, directional emissivity; snow and ice; thermal infrared; surface temperature; snow grain size, remote sensing;

To be submitted to “SIGMA special issue” of Bulletin of Glaciological Research (BGR) as a category of “Article”

Abstract:

The potential of the thermal infrared (TIR) remote sensing for discriminating surface snow types was examined by analyzing TIR radiances acquired from space over the Greenland ice sheet. The brightness temperature difference (BTD) between TIR wavelengths of 11 and 12 μm was found to increase in accordance with in situ observed evolutions of surface snow type. Spatial and temporal distributions of BTD over the entire ice sheet indicated that BTD has a sensitivity of about 1.2 K for variations of the possible snow types. The observed behaviors of BTD were coincident with those predicted by a radiative transfer calculation using previous in situ measured snow emissivities, although some biases on the order of 0.1–0.3 K remain. The dependence of BTD on the surface snow type was also consistent with the behaviors of snow reflectance at the shortwave infrared (SWIR) wavelength 1.6 μm, which is a measure of snow grain size, except for the case of melting wet snow. The inconsistency in the wet snow case was considered to be due to the different optical responses of the TIR and SWIR signals to wet snow, which suggested the possibility of using TIR signals to discriminate wet/dry conditions of snow cover in an old stage. As a result, it is determined that TIR remote sensing has potential not only as an approach supplementary to the SWIR method for assessing surface snow types in daytime but also as the only method for simultaneous retrieval of snow type and surface temperature in nighttime.

1. Introduction

Snow- and ice-covered surfaces in the cryosphere are important targets to be observed for estimating Earth's radiation budget and hydrological cycles. Shortwave reflectance in the visible to shortwave-infrared wavelengths and longwave emission in the mid- to thermal-infrared wavelengths are two key parameters for determining the radiation balance of the Earth (Warren, 1982). While shortwave reflectance is strongly dependent on the mass fraction of snow impurities and snow grain

size, the longwave radiation emitted from snow and ice surfaces is a function of surface temperature and spectral emissivity, of which the latter also varies depending on surface snow types with diffrent grain size (e.g., Dozier and Warren, 1982; Key et al. 1997, Dozier and Painter, 2004).

In recent times, Arctic sea ice and snow cover extents have been shrinking significantly due to warming of the Arctic region (Stroeve et al., 2007; Derksen and Brown, 2012). Polar ice sheets and ice caps have also undergone rapid thinning (e.g., Zwally et al., 2011). In particular, an unprecedented event occurred in 2012: the entire surface of the Greenland ice sheet became wet on 12–13 July 2012 for the first time in the satellite observation records due to inflow of a warm air mass from the south (Tedesco et al., 2013). Hence, precise estimation of the radiation budget is necessary for detecting such drastic environmental changes in the cryosphere, quantifying the areas and volume of melting ice, and understanding the effects of ice-albedo feedback mechanisms.

The relationships between shortwave albedo and snow physical parameters such as snow grain size and impurities have been studied frequently (Aoki et al., 2000; Stamnes et al., 2007; Aoki, et al., 2007; Hori et al., 2007; Painter et al., 2009; Kuchiki et al., 2009). On the contrary, longwave emission from snow cover is usually considered to exhibit blackbody-like behavior, and the dependences of emissivity on snow type are usually ignored in remote sensing applications. For example, snow emissivity has been assumed to be represented by a fixed-spectrum model among various snow types and not to exhibit angular dependence in the retrieval of surface temperature (e.g., Hall et al., 2008). However, as Hori et al. (2006) demonstrated by in situ observations, snow emissivity varies depending on wavelength, snow type, and exitance angle. Thus, the dependence of snow emissivity on snow type and exitance angle has to be taken into account in an analysis of the Earth's radiative balances over the polar region (Dybkjær et al., 2012). Snow emissivity is also an indispensable boundary condition for estimating the thermal emissive properties of the ground surface for polar-night cloud detection (Yamanouchi et al., 1987; Kadosaki et al., 2002).

70 The spectral emissivity of snow has been studied by theoretical simulations, laboratory experiments,
71 and in situ observations. Dozier and Warren (1982) conducted simulations of the
72 directional-hemispherical reflectance of snow and indicated significant angular dependence but little
73 snow grain size or density dependence of snow emissivity. Salisbury et al. (1994) then demonstrated
74 the dependence of snow emissivity on snow types with different grain sizes by laboratory
75 experiments. Wald (1994) proposed several theoretical approaches for simulating snow-type
76 dependent snow emissivity and pointed out that cementation effects, that is, whether snow is welded
77 or disaggregated, are important for modeling the emissivity of snow. Hori et al. (2006) demonstrated
78 the angular and snow-type dependences of snow emissivity by in situ observations. Recently, Hori et
79 al. (2013) succeeded in modeling the measured in situ emissivity spectra of five different snow types
80 with various grain sizes using a semi-empirical approximation approach and found that areal fraction
81 of snow grains with specular facets being exposed to the whole sky are key to characterize the spectral
82 snow emissivity.

83 A typical feature of spectral snow emissivity is seen at wavelengths λ = 11–13 μm where the
84 emissivity has a spectral contrast with a local maximum at λ = 10.5 μm and a local minimum at λ = 13
85 μm (Salisbury et al., 1994). The spectral contrast is enhanced as snow cover evolves from a type of
86 disaggregated snow, such as fine snow or medium and coarse melt forms, to welded snow such as sun
87 crust and bare specular ice. Hence, snow-type dependent emissivity produces a brightness temperature
88 difference (BTD), for example, between MODIS channels 31 (λ = 10.8 μm) and 32 (12.0 μm), that
89 depends on the surface snow type. Thus, snow-type dependent emissivity is potentially usable not only
90 for enhancing the accuracy of surface temperature retrieval but also for discriminating snow types
91 (e.g., Tonooka and Watanabe, 2005; Hori et al., 2006; Hori et al., 2013).

92 As mentioned above, shortwave reflectances at near-infrared (NIR) to shortwave infrared (SWIR)
93 wavelengths around λ = 0.8–1.6 μm have been primarily used for discrimination of snow types with
94 various snow grain sizes (e.g., Stamnes et al. 2007; Painter et al., 2009). However, the NIR and SWIR

methods are only applicable to daytime observations when solar insolation is available. The approach using thermal infrared (TIR) radiance could not only be an alternative or additional approach for sensing snow types in the daytime but also a unique approach for assessing snow types and surface temperature in the nighttime. The possibility of assessing snow types using the TIR method has been examined based solely on satellite observation data (Tonooka and Watanabe, 2005). However, no study has verified the possibility by using data from simultaneous in situ snow pit observations and satellite observations.

This study preliminarily investigates the snow-type dependence of thermal infrared signals from snow cover by comparing satellite-derived BTDs with simulated ones and with in situ observations of snow types. Firstly, we simulate thermal infrared radiances at the top of the atmosphere (TOA) using a radiative transfer (RT) calculation code. Secondly, BTD signals of snow covers are extracted from satellite-observed radiances using Moderate Resolution Imaging Spectroradiometer (MODIS) data. Target areas of the satellite data analysis are confined to homogeneous snow covers over the Greenland ice sheet. Finally, the behaviors of BTD derived from MODIS are compared with the RT simulations and the in situ observational data and also with MODIS-observed snow reflectance at SWIR to examine whether the BTD signals actually exhibit snow-type dependences.

Section 2 of this paper provides a brief review of the spectral emissivities in the TIR wavelength region for various surface types. Then, section 3 explains the methods of the TOA radiance simulations by radiative transfer (RT) code, in situ observations, and satellite data analysis. Section 4 describes the results of the RT simulation and the match-up analysis of satellite data with in situ observations and then discusses the possibility of using satellite-derived BTD signals to discriminate snow types. Finally, section 5 summarizes and concludes this paper.

2. Snow emissivity in the thermal infrared wavelengths

Fig. 1
半幅

Figure 1 indicates TIR spectral emissivities of various forms of ice and water, that is, snow with various grain sizes, bare ice, distilled water, and surface hoar; all spectra are from the ASTER spectral library (1999). The response functions of the MODIS TIR channels are also plotted in the figure (MCST, 2002). In this study, the names of snow types, except for fine new snow case, are basically based on the international classification of snow crystals (Fierz et al., 2009).

The characteristics snow emissivities can be summarized as follows. Fine new snow has high emissivity close to that of a blackbody surface (ε = 1) and exhibits less wavelength dependence. As snow grains evolve and becomes coarser, the areal fraction of the specular facet on individual ice particles increases and the emissivity at wavelengths longer than 11 μm becomes lower due to the enhancement of specular reflectance in the Reststraulen band (Hapke, 1993; Hori et al. 2013). As a result, a spectral contrast appears in the λ = 11–12 μm spectral range. The spectral contrast is enhanced further as the exitance angle increases (not shown in the figure). Finally, bare specular ice has extremely low emissivities, which are the lowest among surfaces made by ice material and can be completely predicted by the Fresnel reflectance formula (Hori et al., 2006). Surface hoar consists of fine acicular ice particles and has high emissivity (even higher than that of fine snow) with a flat spectrum at λ = 11–12 μm. Therefore, the spectral features of surface hoar with the lower spectral contrast are also expected to be usable for discriminating it from other types of snow cover.

It should be noted that the emissivities shown in Fig. 1 are considered valid for only snow cover in the dry stages. When snow cover becomes wet (a slush-like condition) at the melting temperature of ice, emissivities could deviate from those of typical snow spectra and become close to intermediate between those of melt forms and water as measured by Salisbury et al. (1994). Hence, wet snow also exhibits less spectral contrast at λ = 11–12 μm, which might make snow-type discrimination with the TIR-BTD signal difficult and complex (unfortunately, digital data of the wet snow spectrum are not available in the ASTER spectral library and hence not shown in Fig. 1). This wet-snow effect on the TIR emissive behaviors of snow cover is a discussion point in this study.

144

145 ## 3. Methods

146 ### 3.1 Simulation of TOA brightness temperature differences

147 Brightness temperatures (BTs) to be observed by MODIS at various satellite zenith angles (0–60°)
148 were simulated using radiative transfer (RT) code MODTRAN (Berk et al., 1998) for various surface
149 types of hoar, snow, and ice. The effects of the different surface types on BTs were examined by
150 exchanging ground reflectances (i.e., 1 – emissivity) which were used as a boundary condition in this
151 RT simulation. The directional emissivity spectra of snow as the boundary condition were employed
152 from those measured by Hori et al. (2006), the spectral data of which were taken from the Japan
153 Aerospace Exploration Agency (JAXA) in situ data archive for the GCOM mission (2012), and
154 covered types of fine snow (in situ measured median diameter of snow grains by Hori et al. (2006) of
155 d = 70 μm), medium melt forms (d = 600 μm), coarse melt forms (d = 800 μm), sun crust (d = 1100
156 μm), and bare smooth ice. A measured emissivity spectrum of surface hoar is available at only the
157 near-nadir exitance angle of 10° in the ASTER spectral library (1999); thus, BT signals of surface hoar
158 were calculated under the assumption that the measured emissivity at the near-nadir exitance angle
159 was valid at all exitance angles of 0–60°.

160 As mentioned in the previous section, no emissivity spectra of wet snow are available in digital form
161 (only the spectrum measured at the near-nadir angle of 10° was depicted in the figure of Salisbury et
162 al., 1994). In this study, we inferred the existence of wet snow in MODIS data by examining the
163 brightness temperature at λ = 11 μm (BT11) and the reflectance at the SWIR λ = 1.6 μm (Ref1.6). The
164 former (BT11) can be used as a direct indicator of the thermal condition of snow cover, whereas the
165 latter (Ref1.6) varies depending on snow grain size at the top surface and thus the variation of Ref1.6
166 can be interpreted as the change of surface snow type. In addition, the penetration depth of light at λ =
167 1.6 μm is within a depth of 1 cm (Li et al., 2001) which is shallower than those at shorter wavelengths

and close to the skin depth of TIR radiation. Thus, Ref1.6 was used in this study to assess the change of surface snow type and compared with TIR emissive behaviors of snow cover. That is why both the BT11 and Ref1.6 signals were used as measures of snow melting, that is, when BT11 is high (around 272 K) and Ref1.6 is low (around 1-2 %, both values are inferred from two-dimensional scatter plot of MODIS-derived data as will be shown in section 4.3 (Fig. 8)), it is considered a sign of snow melting.

The atmospheric profile in the RT simulation was assumed to be the subarctic summer model, which is stored in the MODTRAN package except for the settings of the air temperature profile and column precipitable water. The air temperature profile near the surface, at altitudes lower than 9 km, was adjusted to make the surface air temperature the same as the employed snow surface temperature. The simulations were performed for the surface temperature range of −50 to 0 °C at an interval of 3°C. For simplicity of simulation in this preliminary study, precipitable water in the column air was assumed to be zero because the target area of the satellite data analysis was located in a high-latitude polar region and the in situ observation site (SIGMA-A, see next section for details) was located at an elevation of 1490 m a.s.l. on the ice sheet. Hence, the effect of precipitable water in the column air on BTD was expected to be small (sensitivity analyses showed that the effect of precipitable water is less than 0.15 K for the five snow types examined in this study in the case of exitance angle of 15° and surface temperature of −5 °C when considering half of the maximum precipitable water in the column air).

Finally, the simulated spectral radiance at TOA was convolved with the channel response functions of the MODIS sensor to generate channel radiances from which the brightness temperatures ($BT11_{sim}$ and $BT12_{sim}$) to be measured at MODIS TIR channels at λ =11 μm and 12 μm were converted with the Planck function. The brightness temperature difference (BTD_{sim}) was then derived by $BT11_{sim} - BT12_{sim}$. These RT calculations were performed for the six surface snow and ice types employed in this study and then compared with actual MODIS data acquired over the Greenland ice sheet.

3.2 In situ observations

Ground-truth observations were conducted at a field campaign site named “SIGMA-A” (78°03′06″ N, 67°37′42″ W, 1490 m a.s.l.; see Aoki et al., 2014 for details), which is located at the northwestern part of the Greenland ice sheet near Qaanaaq, as depicted in Fig. 2, during 26 June to 16 July 2012. The in situ measurement items used in this study were snow physical parameters (snow type and grain size) obtained by snow pit works, various meteorological and optical parameters measured with automatic weather station (AWS) instruments, and whole-sky images taken with a sky-camera system. Clear weather conditions at the SIGMA-A site were identified by examining the downward longwave radiation flux and sky-camera images in order to select the best satellite data without cloud contamination for the comparison with the ground-truth data. In addition, micro-photos of snow particles sampled at the top surface by snow pit work were used for examining the dependence of satellite-derived BTD on snow type.

Fig. 2
半幅

3.3 Satellite data analysis

MODIS Level-1B calibrated radiance data of non-map projected granule scene (product ID: MOD021KM, MOD02SSH) and geolocation data (MOD03) were obtained from NASA’s data archive LAADS web (http://ladsweb.nascom.nasa.gov/). MOD021KM (spatial resolution of 1 km) and MOD03 were used for extracting radiances at the SIGMA-A site for daily match-up analysis with in situ data, whereas MOD02SSH (5-km sampled data) were used for an extensive analysis of the spatial and temporal variations of BTD over the entire Greenland ice sheet. In the latter extensive analysis, the daily 5-km resolution granule scene data were resampled onto a 910×910 grid of a polar stereographic (PS) projection covering the Northern Hemisphere (NH) with a 10-km grid interval at the pole by the nearest-neighbor resampling method. Then, a weekly composite of the PS projection data was generated using seven daily NH data. If multiple observational data from different orbits

overlapped on the same grid cell within the composite period of one week, the earlier observation was selected as the single representative. The analysis periods were from 27 June to 19 July 2012 for the daily match-up analysis and the sun-lit season from April to September of the same year for the weekly analysis of the entire ice sheet.

Satellite-derived brightness temperatures at MODIS TIR channels at λ =11 μm and 12 μm ($BT11_{sat}$ and $BT12_{sat}$) and BTD ($BTD_{sat} = BT11_{sat} - BT12_{sat}$) were derived from TIR channel radiances using the Planck function in the same way as in the RT simulation. Reflectance at SWIR ($Ref1.6_{sat}$) was calculated by the equation $Ref1.6_{sat} = L * \pi / F_0 / \cos\theta_0$, where L and F_0 are the radiance and extra-terrestrial solar irradiance at MODIS channel 6 (λ = 1.6 μm), respectively, and θ_0 is the solar zenith angle. Reflectances at other MODIS channels at visible (VIS), near infrared (NIR), and SWIR wavelengths were derived in the same way, and snow cover pixels were then identified based on several threshold tests of those reflectances and TIR BTs by masking cloudy area and detecting snow signatures in the spectral data, a method similar to that of Stamnes et al. (2007). In the satellite data analysis, pixels of the non-snow land surface classes (e.g., forest, bare land, open water, and so on) were eliminated to extract the BTD_{sat}, $BT11_{sat}$, and $Ref1.6_{sat}$ signals from pure homogeneous snow and ice covers.

Finally, satellite-derived signals of BTD_{sat}, $BT11_{sat}$, and $Ref1.6_{sat}$ acquired at the near-nadir angles of 0–34° and 0–30° were extracted and used in the analysis of the match-up analysis and the extensive analysis, respectively, in order to examine the snow-type dependence of the BTD signals separately from the angular dependence.

4. Results and Discussions

4.1 Simulated TOA brightness temperature differences

Fig. 3
全幅

Figure 3 indicates the brightness temperature difference (BTD_{sim}) as functions of surface temperature and satellite zenith angle simulated by MODTRAN for the six surface types. Basically, BTD_{sim}

exhibited a tendency to decrease as the surface temperature decreased because of the nonlinear response of the Planck function to the surface temperature. Except for the surface temperature dependence, BTD_{sim} clearly exhibited a tendency to increase as the snow type evolved in the order of surface hoar, fine snow, medium melt forms, coarse melt forms, welded snow, and bare ice. For example, BTD_{sim} values at near-nadir sensor zenith angles of around 0–10° and at surface temperatures warmer than −10°C were around 0.15 K for surface hoar, 0.45 K for fine snow, 0.75 K for medium melt forms, 0.9 K for coarse melt forms, 0.93 K for sun crust, and 1.8 K for bare specular ice. As expected from the emissivity spectra in Fig. 1, bare specular ice had the largest BTD_{sim} among the surface types examined. When remotely sensing snow surfaces at large sensor zenith angles, the effect of angular dependence could be significant for the case of bare smooth ice (this angular dependence is not discussed further in this paper).

4.2 Match-up data analysis (comparison with in situ data)

Figure 4 shows images of MODIS match-up data (MUD) at the SIGMA-A site observed during the ground observation period. The parameters shown in the figure are the following: (a) true-color RGB composite, (b) false-color RGB composite, (c) SWIR reflectance at λ = 1.6 μm ($Ref1.6_{sat}$), (d) brightness temperature at λ = 11 μm ($BT11_{sat}$), and (e) brightness temperature difference between the 11-μm and 12-μm channels (BTD_{sat}). The location of the SIGMA-A site is the center pixel within the box depicted in the individual images. From these images, snow grain size as inferred from $Ref1.6_{sat}$ at the SIGMA-A site was found to change from one day to the next in accordance with the surface temperature. For example, snow grain size decreased (i.e., $Ref1.6_{sat}$ increased) on 5 July when the surface temperature ($BT11_{sat}$) decreased to 270.5 K, and snow grain size then increased on 16 July when $BT11_{sat}$ increased to 272 K. BTD_{sat} also exhibited daily changes following the variations of the possible snow surface.

Fig. 4
全幅

During the ground observation period, characteristic meteorological events were actually observed at the SIGMA-A site. First, surface hoar formation was observed at the surface on 4–5 July. In addition, a rainfall event occurred on 10–13 July. Figure 5 indicates the temporal variations of $Ref1.6_{sat}$, $BT11_{sat}$, and BTD_{sat} extracted from the center pixel of the MUD images (in the middle plot). Error bars denote the maximum and minimum values within the surrounding eight pixels. Temporal series of air temperature and downward longwave radiation flux measured by AWS (in the upper plot) and micro-photos of snow particles sampled at the surface (in the bottom pictures) are also shown. As described in the explanations of the MUD images, the snow grain size and crystal shape shown in the micro-photos of Fig. 5 changed from day to day. For example, snow grains first had faceted crystal shapes on 2 July. Then, acicular surface hoar formed on 4–5 July and was suddenly transformed to wet-melt-forms shape on 6 July when the air temperature increased to above 0°C. The size of the snow grains on 8–9 July was similar to that of the faceted crystals seen on 2 July, although the faceted feature seen on 2 July had disappeared by 8–9 July. Finally, the snow grains were found to have evolved to giant melt forms on 14 July, after the rainfall event.

Fig. 5
全幅

Satellite-derived BTD_{sat} followed the temporal evolutions of snow crystal shape coincident with $Ref1.6_{sat}$ and $BT11_{sat}$ except for 6 July when melting of surface hoar occurred. The responses of BTD_{sat} to $BT11_{sat}$ and $Ref1.6_{sat}$ are more clearly shown in the scatter plot of Fig. 6. Simulated relations between $BT11_{sim}$ and BTD_{sim} are also shown by the dashed line in the figure. Data points in the scatter plots can be classified roughly into four groups in terms of BTD_{sat} and snow grain size; 1) medium to coarse faceted crystals and melt forms observed on 30 June and 2 and 8–9 July before and after the surface hoar formation on 4–5 July, 2) surface hoar on 5 July, 3) melting wet surface hoar (transforming to melt forms) on 6 July, and 4) giant melt forms after the rainfall on 11 July.

Fig. 6
全幅

The first group of medium to coarse faceted crystals on 30 June and 2 July exhibited moderate $Ref1.6_{sat}$ of 2.4–3.6% and BTD_{sat} of 0.6–0.7 K, of which the latter was slightly lower than the simulated BTD_{sim} of medium melt forms (biases are estimated to be 0.1 K) or corase melt forms (0.3

290 K). BTD_{sat} of the second group (surface hoar observed on 5 July) was the lowest value (center pixel:
291 0.47 K, min–max of the surrounding pixels: 0.31–0.51 K), the range of which was close to or even
292 lower than the BTD_{sim} line of fine snow (but not on the surface hoar line). The depression of BTD_{sat}
293 occurred coincidently with the increase of $Ref1.6_{sat}$ to 6.3%, indicating the change of the surface snow
294 type to finer snow. The third group of melting wet surface hoar was observed on 6 July when $Ref1.6_{sat}$
295 suddenly decreased to 2.2% and the air temperature became high, above the melting point of ice, (even
296 the adjacent night temperature was high at around 0°C) but BTD_{sat} did not change much (center: 0.48
297 K, min–max: 0.4–0.66 K). Then, on 8–9 July, BTD_{sat} returned to 0.6–0.7 K, the same level as for the
298 first group of medium to coarse faceted crystals seen on 2 July, and was accompanied by a slight
299 increase in $Ref1.6_{sat}$ (2.6–3.3%). Finally, after the rainfall event on 10–13 July, BTD_{sat} of the fourth
300 group (giant melt forms) increased further to 0.9–1.0 K, which were the highest values, close to the
301 BTD_{sim} line of coarse melt forms, during the in situ observation period and which were coincident with
302 the lowest $Ref1.6_{sat}$ (around 1.4%). Hence, except for 6 July when the snow surface was considered to
303 have become wet under the warm air temperature condition, the behaviors of BTD_{sat} were coincident
304 with those of $Ref1.6_{sat}$. Thus, the snow grain size of the top surface is considered to affect both the
305 BTD_{sat} and $Ref1.6_{sat}$ signals.

306 The inconsistency seen between $Ref1.6_{sat}$ and BTD_{sat} on 6 July is possibly due to the different
307 responses of the signals to variations of snow water content. As explained in Section 2, wet snow has a
308 high and flat emissivity spectrum in TIR (Salisbury et al., 1994). Thus, BTDs of wet snow are
309 expected to be lower than those of dry snow, which may have led to the low BTD_{sat} signals observed
310 on 6 July.

311 Unfortunately, high BTD_{sat} comparable to that of the sun crust type was not observed at the
312 SIGMA-A site during the AWS operation period in the in situ observation period (29 June–16 July).
313 However, partial formations of sun crust on the surface were recorded by observers at the SIGMA-A
314 site on 17 June and 8 July when sunny and clear-sky weather conditions existed (Tanikawa et al.,

315 2014). MODIS-derived MUD images indicated that BTD_{sat} actually exceeded 1.0 K at parts of the ice
316 sheet surface around the SIGMA-A site on both days, although BTD_{sat} at the center pixel of 8 July
317 does not exhibit such a high value, possibly due to spatial heterogeneity of snow type within the
318 1-km-size MODIS pixel. The observed high BTD_{sat} areas indicate the potential of the TIR-BTD
319 method for detecting large-scale formations of sun crust on the ice sheet.

320 As a result of the MUD analysis, the snow-type dependent behavior of BTD_{sat} was found to be
321 basically consistent with that of BTD_{sim}, derived in Fig. 3, although there were some biases on the
322 order of 0.1–0.3 K between BTD_{sat} and BTD_{sim}, as shown in Fig. 6 (a). The remaining BTD biases are
323 possibly due to 1) calibration error of the satellite sensor, 2) atmospheric effects (water vapor
324 absorption and/or invisible thin cirrus cloud covers), and 3) spatial heterogeneity of the surface snow
325 type. To further explore the potential of the TIR-BTD method, the relationship between BTD_{sat} and
326 $BT11_{sat}$ or $Ref1.6_{sat}$ is examined on a much wider spatial scale in next section using MODIS data of the
327 entire Greenland ice sheet.

328

329 **4.3 Observed brightness temperatures over the Greenland ice sheet**

Fig. 7
全幅

330 Figure 7 indicates the spatial distributions of BTD_{sat}, $BT11_{sat}$, and $Ref1.6_{sat}$ over the entire Greenland
331 ice sheet observed during (a) 2–8 April, (b) 11–17 June, and (c) 16–22 July 2012. Figure 8 shows
332 two-dimensional scatter plots for $BT11_{sat}$–BTD_{sat} and $Ref1.6_{sat}$ –BTD_{sat}, which were extracted from the
333 images shown in Fig. 7. In Fig. 8, the RT-simulated relationships between $BT11_{sim}$ and BTD_{sim} for five
334 surface types including surface hoar, fine snow, medium melt forms, coarse melt forms, and sun crust
335 (bare ice is not shown in the figure because the plot of bare ice is out of the vertical axis range) are
336 also plotted with dashed lines.

337 Characteristic seasonal variations of BTD_{sat} are clearly seen in Figs. 7 and 8. That is, in spring (2–8
338 April) when the surface temperature was colder than 260 K, BTD_{sat} was confined to low values of

339 0.1–0.3 K, which indicates the existence of surface hoar and/or fine snow, as shown in Fig. 8(a). Then,
340 in the early summer (11–17 June), BTD_{sat} gradually increased as the surface became warmer. Marginal
341 regions of the ice sheet exhibited higher BTD_{sat} values of around 0.6 K, indicating snow evolution to
342 medium melt forms, whereas central inland regions exhibited low BTD_{sat}, which is a sign of surface
343 hoar formation. In mid-summer (16–22 July), southern parts of the ice sheet surface exhibited very
344 high BTD_{sat} of more than 1.2–1.4 K, whereas $BT11_{sat}$ ranged near the melting point of ice, indicating
345 the occurrence of drastic snow-type evolution from medium and coarse melt forms to welded sun crust.
346 As an extreme state, as $BT11_{sat}$ became close to the melting point of ice, BTD_{sat} was found to decrease
347 steeply at the marginal ice sheet (particularly at the western side). This depression of BTD_{sat} is not
348 explainable by the snow-type dependent emissivity in dry stages shown in Figs. 1 and 3 but rather
349 possibly due to the presence of wet snow, which reduces the TIR spectral contrast in emissivity, as
350 was also seen in the MUD analysis.

Fig. 8
全幅

351 The spatial pattern of BTD_{sat} seen in Fig. 7 is basically coincident but of opposite sign with $Ref1.6_{sat}$,
352 which is similar to the one seen in Figs. 4 and 6 with much wider ranges of variation of 0.1–1.3 K,
353 except for the possible wet snow region. Thus, BTD_{sat} is considered to have potential for detecting
354 snow cover evolution at the scale of the entire Greenland ice sheet with a sensitivity of about 1.2 K for
355 the variations of possible snow types. In addition, as seen above, BTD_{sat} became very low, down to
356 around the same level as the surface hoar, at around 0.2 K at the marginal zone of the ice sheet where
357 $Ref1.6_{sat}$ was less than 2% and $BT11_{sat}$ was nearly at the melting point of ice. Thus, the response of the
358 BTD_{sat} and $Ref1.6_{sat}$ signals to wet snow seems to be different, as already discussed in the previous
359 section.

360 From the figures shown above, two common features of the BT11-BTD relationship in response to
361 the surface snow conditions were extracted. One is the (positive) correlation when the surface
362 temperature is below the melting point of ice, i.e., the snow cover is in a dry snow stage. The second is

363 the steep negative correlation when the surface temperature is at or near the melting point of ice and
364 thus the snow cover is in a wet snow stage.

365 The positive correlation is directly explained by the feature of the snow-type dependent emissivity.
366 That is, when the surface temperature is low and the snow surface is covered with disaggregated fine
367 ice particles, the emissivity is high and thus BTD is low. As a special lower limit case, extremely low
368 BTD signals accompanied by moderate Ref1.6 of around 7–8% can be an indicator of the formation of
369 surface hoar. When the surface temperature becomes warmer and as the surface snow grains become
370 coarser and welded, the emissivity decreases and the spectral contrast at λ = 11–12 μm is enhanced,
371 leading to the increase in the BTD signals.

372 The latter steep negative correlation seen in Fig. 8 is considered to be due to the drastic transition of
373 the surface snow type from sun crust to wet slush snow in the melting wet snow stage. When the
374 surface is covered with specular sun crust, the BTD signal can be higher than 1.0 K even at a surface
375 temperature near the melting point of ice because the top surface of the sun crust could be dry due to
376 radiative cooling under a clear-sky condition. However, once the sun crust collapses due to further
377 warming of the air temperature, the surface becomes wet and further slush conditions could appear.
378 Hence, the surface is considered to no longer exhibit a specular nature but rather to become close to
379 the wet snow surface exhibiting high emissivity measured by Salisbury et al. (1994). The low Ref1.6
380 and high BT11 at the marginal ice sheet also clearly indicate the occurrence of such melting wet snow
381 cover. In addition, if the surface is covered with a mixture of wet snow and open water, such as melt
382 pond or river flows of melted water flowing down to the coastal area, such low BTDs might also result
383 similarly.

384 Another possibility for the extremely low BTD at the marginal ice sheet is the existence of many
385 small cavities on the surface, such as the cryoconite holes that have been observed frequently on the
386 ice sheet surface in summer (e.g., Takeuchi et al., 2000). A rough surface condition including

cryoconite holes might make the ice sheet surface a porous medium as a whole; hence, the surface may act as an effective blackbody-like radiator with a high and flat spectral emissivity. To explore and understand the cause of the extremely low BTDs at the melting marginal ice sheet, further in situ observation coincident with satellite observation is necessary.

Finally, while the negative correlation between BT11 and BTD seems to occur coincident with drastic evolution of snow type from sun crust to wet snow, Ref.1.6 is less sensitive to such snow type variations. This may indicate an advantage of using the BT11–BTD relation to assess the evolution of snow type and even the degree of wetness of the top surface in such an old melting-snow stage. For isolating the wet snow cover from the clusters in Fig. 8, further in-situ observation of the spectral-directional emissivity of wet snow would be helpful. As Tanikawa et al. (2014) indicated, the degree of polarization of reflected light at around λ =1.6 μm could also be an alternative way to assess snow-type change instead of simple SWIR reflectance.

5. Summary and Conclusion

This study examined the sensitivity of thermal infrared (TIR) brightness temperature difference (BTD) signals over the Greenland ice sheet to variations of surface snow type. Radiative transfer (RT) calculations using MODTRAN code for various surface types indicated that BTD measured at the top of the atmosphere can vary in the range of 0.15–1.8 K (for near-nadir angle cases of 0–10°) depending on variations of the surface snow type among surface hoar, fine snow, medium melt forms, coarse melt forms, sun crust, and bare specular ice. The behaviors of satellite-observed BTDs were actually correlated with the evolutions of in situ observed snow types from surface hoar, to medium and coarse melt forms, to giant melt forms, the existence of which was confirmed by micro-photos taken at the ground observation site. In addition, satellite-observed BTDs over the entire Greenland ice sheet exhibited spatial and temporal variations in the ranges of 0.1–1.3 K in accordance partly with

411 variations of shortwave infrared reflectance, which are a measure of snow grain size. Therefore,
412 although there is still a bias between satellite-derived BTDs and simulated ones that is currently
413 estimated to be 0.1–0.3 K, BTD has a sensitivity on the order of 1.2 K at near-nadir angle cases for the
414 discrimination of various surface snow types from space.

415 The key features to be considered for understanding the snow-type dependent behaviors of BTD are
416 the following:

417 1) When the snow type changes from disaggregated fine new snow to coarse melt forms and welded
418 sun crust in a dry snow stage, BTD is positively correlated with BT11.

419 2) When the snow type changes from sun crust to wet slush snow in a wet snow stage, BTD is
420 negatively correlated with BT11.

421 3) Wet slush snow possibly has the lowest BTD, which is close to the BTD range of surface hoar.

422 4) Large-scale formation of surface hoar seems to occur and exhibit low BTD of 0.2–0.3 K in inland
423 areas over the ice sheet in a surface temperature range below the melting point of ice even in
424 summer.

425 Using a two-dimensional scatter plot between BT11 and BTD, the type of snow can be categorized
426 into several classes such as dry snow, wet melting snow, and surface hoar. The dry snow can be
427 further classified into several sub-classes with different grain sizes, including sun crust or bare ice at
428 the extreme case.

429 The observed behaviors of BTD are understandable by the changes of snow types inferred from the
430 reflectance at λ = 1.6 μm (Ref1.6), except for the case of melting wet snow. The inconsistency
431 between the BTD and Ref1.6 behaviors is considered to be due to different responses to variation of
432 snow water content at the top surface, which may indicate the possibility of assessing wet/dry

conditions and even the degree of wetness of the snow surface in the old snow stage using the BT11–BTD relationship.

As a result of this study, it is shown that snow types can be discriminated not only from radiances at near-infrared to shortwave-infrared wavelengths but also from those at TIR. For more precise snow-type discrimination with the TIR method, additional in situ measurements and simultaneous satellite observations should be carried out, particularly for the wet snow conditions for which the number of in situ observations of emissivity spectra is still limited. In addition, the effects of 1) the uncertainty of satellite sensor calibrations (including long-term sensor degradation), 2) the atmospheric effects (absorption by water vapor and/or invisible thin cirrus clouds), and 3) spatial heterogeneity of the surface snow type on BTD signals have to be quantified in order to reduce the remaining BTD biases seen between satellite observations and RT simulations and also to apply the TIR-BTD method to long-term snow-type analysis on a global scale.

Acknowledgments

This study was supported in part by (1) the Japan Society for the Promotion of Science (JSPS), Grant-in-Aid for Scientific Research (S), number 23221004, (2) the Experimental Research Fund for Global Environment Conservation, the Ministry of the Environment of Japan, (3) the Global Change Observation Mission - Climate (GCOM-C) / the Second–generation GLobal Imager (SGLI) Mission, the Japan Aerospace Exploration Agency (JAXA). The MODIS data used in this study were acquired as part of NASA's Earth-Sun System Division and archived and distributed by the MODIS Adaptive Processing System (MODAPS). Map in Fig. 2 was created by NunaGIS (http://en.nunagis.gl/) operated by Asiaq, Greenland Survey.

456 **References**

457 Aoki, Te., Aoki, Ta., Fukabori, M., Hachikubo, A., Tachibana, Y. and Nishio, F. (2000): Effects of
458 snow physical parameters on spectral albedo and bidirectional reflectance of snow surface. *J.*
459 *Geophys. Res.*, **105**(D8), 10219-10236.

460 Aoki, Te., Hori, M., Motoyoshi, H., Tanikawa, T., Hachikubo, A., Sugiura, K., Yasunari, T. J.,
461 Storvold, R., Eide, H. A., Stamnes, K., Li, W., Nieke, J., Nakajima, Y., Takahashi, F. (2007):
462 ADEOS-II/GLI snow/ice products—Part II: Validation results using GLI and MODIS
463 data. *Remote Sens. Environ.*, **111**, 274−290. doi:10.1016/j.rse.2007.02.035.

464 Aoki, Te., Matoba, S., Yamaguchi, S., Tanikawa, T., Niwano, M., Kuchiki, K., Adachi, K., Uetake, J.,
465 Motoyama, H. and Hori, M. (2014): Light absorbing snow impurity concentrations measured on
466 Northwest Greenland ice sheet in 2011 and 2012. *Bull. Glaciological Res.*, (accepted to the same
467 volume on SIGMA Special Issue).

468 ASTER spectral library (1999): Reproduced from the ASTER Spectral Library through the courtesy of
469 the Jet Propulsion Laboratory, California Institute of Technology, Pasadena, California.
470 Copyright (C) 1999, California Institute of Technology. ALL RIGHTS
471 RESERVED http://speclib.jpl.nasa.gov/

472 Berk, A., Bernstein, L., Anderson, G., Acharya, P., Robertson, D., Chetwynd, J. and Adler-Golden, S.
473 (1998): MODTRAN cloud and multiple scattering upgrades with application to AVIRIS. *Remote*
474 *Sens. Environ.*, **65**, 367-375.

475 Derksen, C. and Brown, R. (2012): Spring snow cover extent reductions in the 2008–2012 period
476 exceeding climate model projections. *Geophys. Res. Lett.*, **39**, DOI: 10.1029/2012GL053387.

477 Dozier, J. and Painter, T. H. (2004): Multispectral and hyperspectral remote sensing of alpine snow
478 properties, *Annual Rev. Earth Planetary Sci.*, **32**, 465-494,
479 doi: 10.1146/annurev.earth.32.101802.120404.

480 Dozier, J. and Warren, S. (1982): Effect of viewing angle on the infrared brightness temperature of
481 snow, *Water Resour. Res.*, **18**, 1424–1434.
482 Dybkjær, G., Tonboe, R. and Høyer, J. L. (2012): Arctic surface temperatures from Metop AVHRR
483 compared to in situ ocean and land data, *Ocean Sci.*, **8**, 959-970, doi:10.5194/os-8-959-2012.
484 Fierz, C., Armstrong, R. L., Durand, Y., Etchevers, P., Greene, E., McClung, D. M., Nishimura, K.,
485 Satyawali, P. K. and Sokratov, S. A. (2009): "The International Classification for Seasonal Snow
486 on the Ground," IHP-VII Technical Documents in Hydrology N°83, IACS Contribution N°1,
487 UNESCO-IHP, Paris.
488 Hall, D. K., Box, J. E., Casey, K. A., Hook, S. J., Shuman, C. A. and Steffen, K. (2008): Comparison
489 of satellite-derived and in-situ observations of ice and snow surface temperatures over
490 Greenland, *Remote Sens. Environ.*, **112**, 3739–3749.
491 Hapke, B. (1993): Theory of reflectance and emittance spectroscopy, Cambridge Univ. Press.
492 Hori, M., Aoki, Te., Tanikawa, T., Motoyoshi, H., Hachikubo, A., Sugiura, K., Yasunari, T., Eide, H.,
493 Storvold, R., Nakajima, Y. and Takahashi, F. (2006): In-situ measured spectral directional
494 emissivity of snow and ice in the 8–14 μm atmospheric window, *Remote Sens. Environ.*, **100**,
495 486–502.
496 Hori, M., Aoki, T., Stamnes, K. and Li, W. (2007): ADEOS-II/GLI snow/ice products— Part III:
497 Retrieved results. *Remote Sens. Environ.*, **111**, 291−336. doi:10.1016/j. rse.2007.01.025.
498 Hori, M, Aoki, Te., Tanikawa, T., Hachikubo, A., Sugiura, K., Kuchiki, K. and Niwano, M. (2013):
499 Modeling angular dependent spectral emissivity of snow and ice in the thermal infrared
500 atmospheric window. *Appl. Opt.*, **52**, 7243–7255.
501 JAXA in-situ data archive for GCOM mission. (2012): Reproduced from the archived in-situ data
502 provided by Japan Aerospace Exploration
503 Agency. http://suzaku.eorc.jaxa.jp/GCOM_C/insitu/index.html

504 Kadosaki, G., Yamanouchi T. and Hirasawa, N. (2002): Temperature dependence of brightness
505 temperature difference of AVHRR infrared split window channels in the Antarctic. *Polar*
506 *Meteorol. Glaciol.*, **16**, 106-115.
507 Key, J. R., Collins, J. B., Fowler, C. and Stone R. S. (1997): High-latitude surface temperature
508 estimates from thermal satellite data, *Remote Sens. Environ.*, **61**, 302-309.
509 Kuchiki, K, Aoki, Te., Tanikawa, T. and Kodama, Y. (2009): Retrieval of snow physical parameters
510 using a ground-based spectral radiometer, *Appl. Opt.*, **48**, 5567-5582.
511 Li, W., Stamnes, K., Chen, B. and Xiong, X. (2001): Snow grain size retrieved from near-infrared
512 radiances at multiple wavelengths. *Geophy. Res. Lett.*, **28**, 1699– 1702.
513 MODIS Characterization Support Team (MCST). (2002): MODIS ProtoFlight Model (PFM) Relative
514 Spectral Response (RSR).
515 ftp://mcst.hbsss-sigma.com/pub/permanent/MCST/PFM_L1B_LUT_4-30-99/
516 Painter, T. H., Rittger, K., McKenzie, C., Slaughter, P., Davis, R. E. and Dozier, J. (2009): Retrieval
517 of subpixel snow covered area, grain size, and albedo from MODIS. *Remote Sens. Environ.*, **113**,
518 868-879.
519 Salisbury, J. W., D'Aria, D. M. and Wald, A. (1994): Measurements of thermal infrared spectral
520 reflectance of frost, snow, and ice. *J. Geophys. Res.*, **99**, 24235– 24240.
521 Stamnes, K., Li,W., Eide, H., Aoki, T., Hori, M. and Storvold, R. (2007): ADEOS-II/GLI snow/ice
522 products — Part I: Scientific basis. *Remote Sens. Environ.*, **111**, 258−273.
523 doi:10.1016/j.rse.2007.03.023.
524 Stroeve, J., Holland, M. M., Meier, W., Scambos, T. and Serreze, M. (2007): Arctic sea ice decline:
525 faster than forecast. *Geophys. Res. Lett.*, **34**. doi:10.1029/2007GL029703.
526 Tanikawa, T., et al. (2014): Spectral Measurement of Degree of Linear Polarization of Snow in the
527 Snowfield (TBD). *J. Geophys. Res.*, (submitted).

528 Takeuchi, N., Kohshima, S., Yoshimura, Y., Seko, K. and Fujita K. (2000): Characteristics of
529 cryoconite holes on a Himalayan glacier, Yala Glacier Central Nepal. *Bull. Glacier Res.*, **17**,
530 51-59.
531 Tedesco, M., Fettweis, X., Mote, T., Wahr, J., Alexander, P., Box, J. and Wouters, B. (2012):
532 Evidence and analysis of 2012 Greenland records from spaceborne observations, a regional
533 climate model and reanalysis data. *The Cryosphere*, **7**, 615-630, doi:10.5194/tc-7-615-2013.
534 Tonooka, H. and Watanabe A. (2005): Applicability of thermal infrared surface emissivity ratio for
535 snow/ice monitoring, *Proc. SPIE* **5655**, 282-290 (January 20, 2005); doi:10.1117/12.579929.
536 Wald, A. (1994): Modeling thermal infrared (2– 14 lm) reflectance spectra of frost and snow. *J.*
537 *Geophys. Res.*, **99**, 24241–24250.
538 Warren, S. G. (1982): Optical properties of snow. *Rev. Geophy. Space Phys.*, **20**, 67–89.
539 Yamanouchi, T., Suzuki, K. and Kawaguchi, S. (1987): Detection of clouds in Antarctica from
540 infrared multispectral data of AVHRR. *J. Meteorol. Soc. Japan*, **65**, 949−962.
541 Zwally, H. J., Jun, LI, Brenner, A. C., Beckley, M., Cornejo, H. G., Dimarzio, J., Giovinetto, M. B.,
542 Neumann, T. A., Robbins, J.; Saba, J. L., Donghui, YI. and Wang, W. (2011): Greenland ice
543 sheet mass balance: distribution of increased mass loss with climate warming; 2003–07 versus
544 1992–2002. *J. Glaciol.*, **57**, 88-102.DOI: 10.3189/002214311795306682.
545

546 **Figure Captions**

547 Fig. 1 Spectral directional emissivity of various surface types in the thermal infrared window region
548 (exitance angle is 10° from the normal) all taken from the ASTER spectral library (1999). Also
549 plotted are response functions of MODIS TIR channels at λ =11.0 μm and 12.0 μm. Snow types
550 are employed according to the international classification of snow crystals (Fierz et al., 2009).
551
552 Fig. 2 Location of in situ observation site at the northwestern part of the Greenland ice sheet
553 (SIGMA-A site: 78°03′ 06″ N, 67°37′42″ W, 1490 m a.s.l.).
554
555 Fig. 3 Simulated brightness temperature differences (BTD_{sim}) between MODIS channels 31 (λ = 11
556 μm) and 32 (λ = 12 μm) at the top of the atmosphere as functions of satellite zenith angle and
557 surface temperature calculated using spectral emissivities for the various snow and water surfaces
558 of (a) surface hoar, (b) fine snow, (c) medium melt forms, (d) coarse melt forms, (e) sun crust,
559 and (f) bare specular ice.
560
561 Fig. 4 Match-up analysis images of (a) MODIS true-color RGB composite, (b) false-color RGB
562 composite, (c) reflectance at the wavelength (λ) of 1.6 μm ($Ref1.6_{sat}$), (d) brightness temperature
563 at λ = 11 μm ($BT11_{sat}$), and (e) brightness temperature difference between MODIS channels 31
564 and 32 ($BTD_{sat} = BT11_{sat} - BT12_{sat}$) observed at the SIGMA-A site during the in situ observation
565 period (2, 5, 6, 8, 9, and 16 July 2012). The SIGMA-A site is located at the center of these images
566 within the box. Color legends for Fig. 4 (c), (d), and (e) are shown at the bottom. In Fig. 4 (e),
567 gray, brown, and blue colors denote clouds, bare land, and open ocean, respectively.
568
569 Fig. 5 (Upper) Temporal series of air temperature (°C) and downward longwave radiation flux (W/m^2)
570 measured with the automatic weather station at the SIGMA-A site during 30 June to 19 July 2012.
571 (Middle) Temporal variations of satellite-derived reflectance at λ = 1.6 μm ($Ref1.6_{sat}$ in %, the
572 value of which is multiplied by 0.1), brightness temperature at λ = 11 μm ($BT11_{sat}$ in Kelvin), and

brightness temperature difference between 11 μm and 12 μm (BTD_{sat} in Kelvin) extracted at the center pixel of the MUD images shown in Fig. 4. Error bars denote the maximum and minimum values within the surrounding eight pixels. (Lower) Micro-photos of surface snow crystals taken at the site.

Fig. 6 Scatter plots of (a) Brightness temperature at λ = 11 μm ($BT11_{sat}$) and brightness temperature difference between 11 μm and 12 μm ($BTD_{sat} = BT11_{sat} - BT12_{sat}$) and (b) reflectance at λ = 1.6 μm ($Ref1.6_{sat}$) and BTD_{sat} extracted from the center pixel of the match-up image in Fig. 4. Error bars denote the maximum and minimum values within the surrounding eight pixels. Also plotted in the left figure are the expected BTD lines, which are averages of the simulated BTD_{sim} at near-nadir satellite zenith angles between 0 and 30° shown in Fig. 3.

Fig. 7 Spatial distribution of brightness temperature difference (BTD_{sat}) between 11 μm and 12 μm (left), brightness temperature at λ = 11 μm ($BT11_{sat}$) (middle), and reflectance at λ = 1.6 μm ($Ref1.6_{sat}$) (right) observed over the Greenland ice sheet in the period of (a) 2–8 April, (b) 11–17 June, and (c) 16–22 July 2012. The black color over the ice sheet denotes remaining cloudy areas that could not be eliminated in the weekly composite period.

Fig. 8 Scatter plot between $BT11_{sat}$ and BTD_{sat} (left column) and $Ref1.6_{sat}$ and BTD_{sat} (right column) extracted from the images shown in Fig. 7 in the period of (a) 2–8 April, (b) 11–17 June, and (c) 16–22 July 2012. Also plotted in the left column figures are the expected BTD lines for the snow types of surface hoar, fine snow, medium melt forms, coarse melt forms, and sun crust, which are averages of the simulated BTD_{sim} at near-nadir satellite zenith angles between 0–30° shown in Fig. 3.

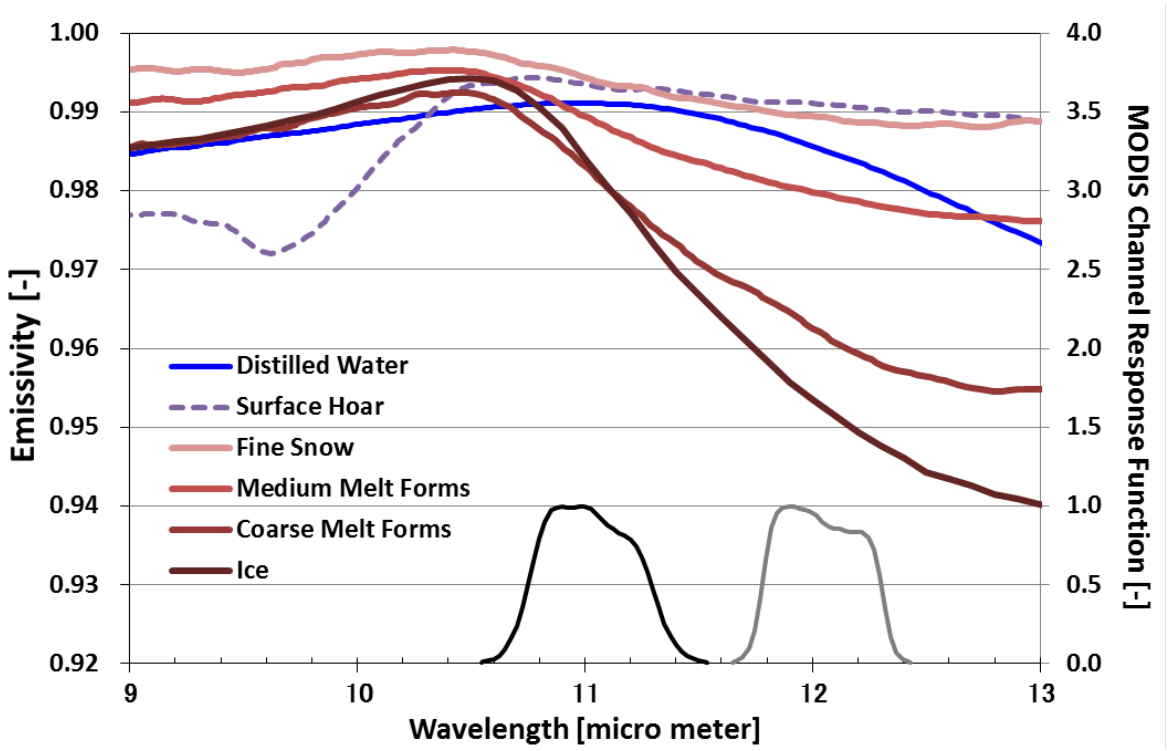

Fig. 1 Spectral directional emissivity of various surface types in the thermal infrared window region (exitance angle is 10° from the normal) all taken from the ASTER spectral library (1999). Also plotted are response functions of MODIS TIR channels at λ =11.0 μm and 12.0 μm. Snow types are employed according to the international classification of snow crystals (Fierz et al., 2009).

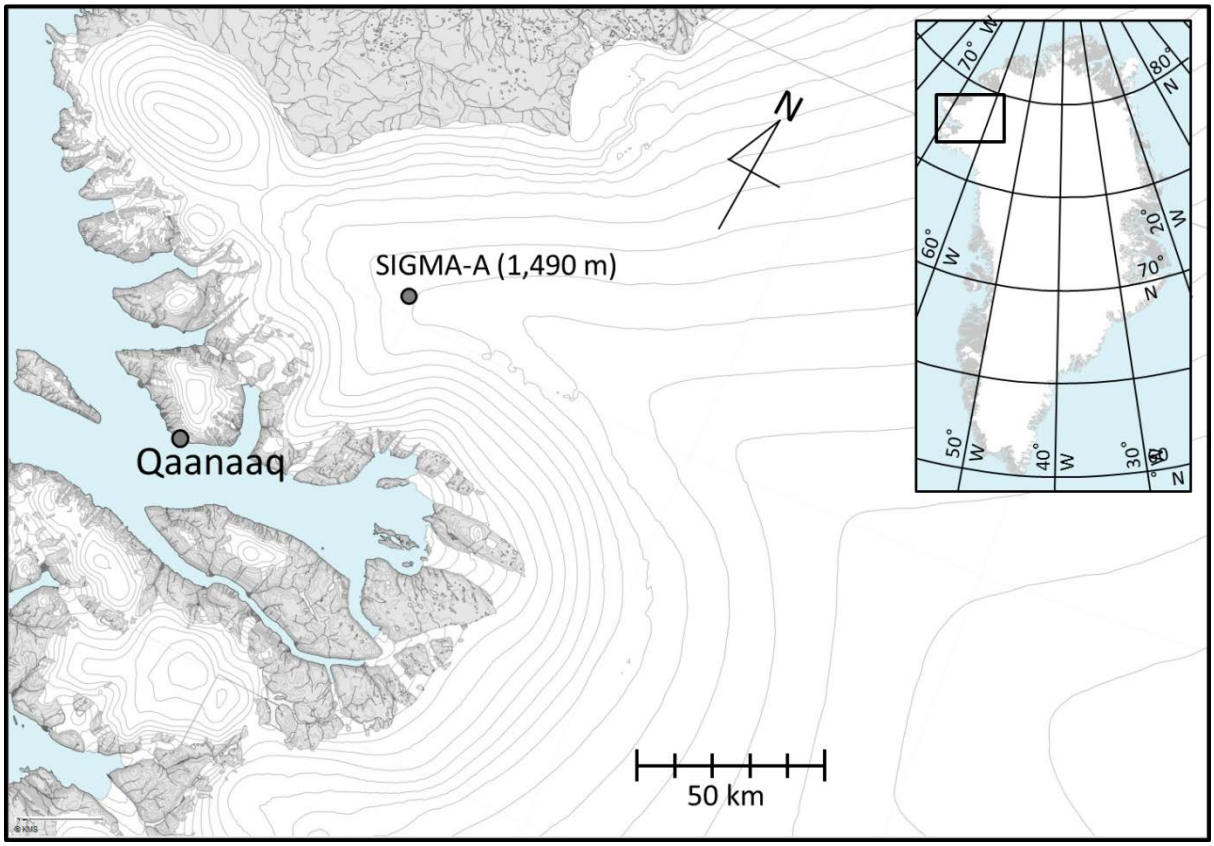

Fig. 2 Location of in situ observation site at the northwestern part of the Greenland ice sheet (SIGMA-A site: 78°03′ 06″ N, 67°37′42″ W, 1490 m a.s.l.).

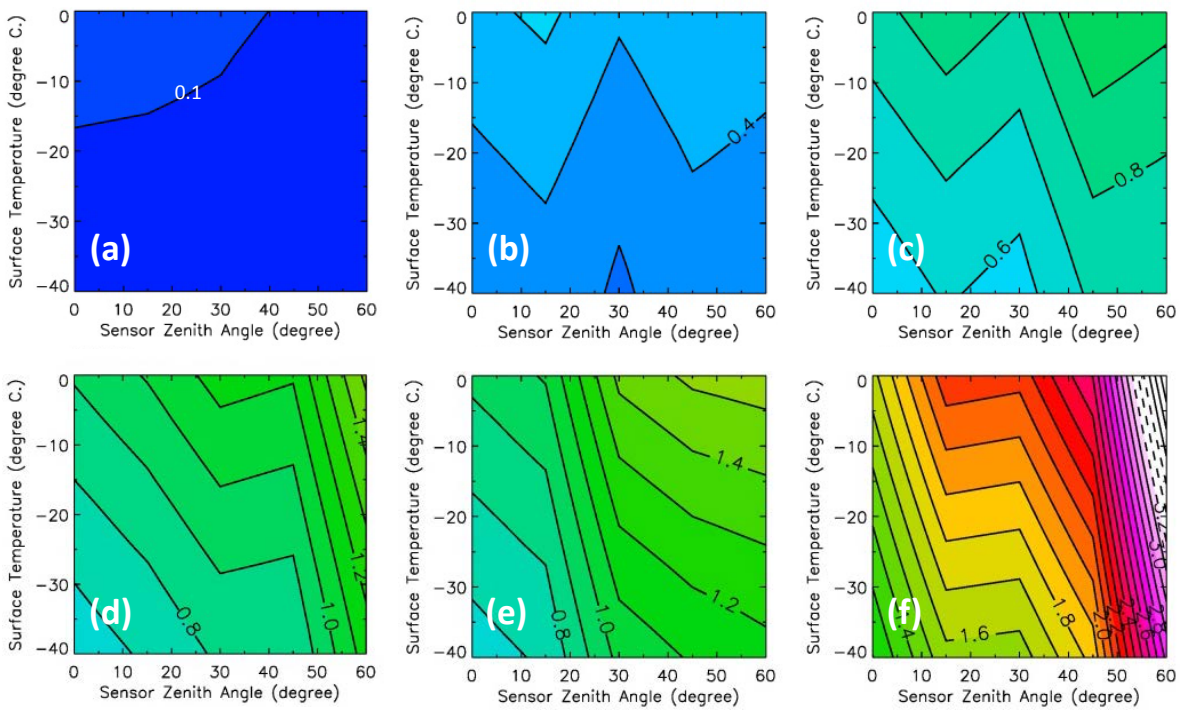

Fig. 3 Simulated brightness temperature differences (BTD_{sim}) between MODIS channels 31 (λ = 11 μm) and 32 (λ = 12 μm) at the top of the atmosphere as functions of satellite zenith angle and surface temperature calculated using spectral emissivities for the various snow and water surfaces of (a) surface hoar, (b) fine snow, (c) medium melt forms, (d) coarse melt forms, (e) sun crust, and (f) bare specular ice.

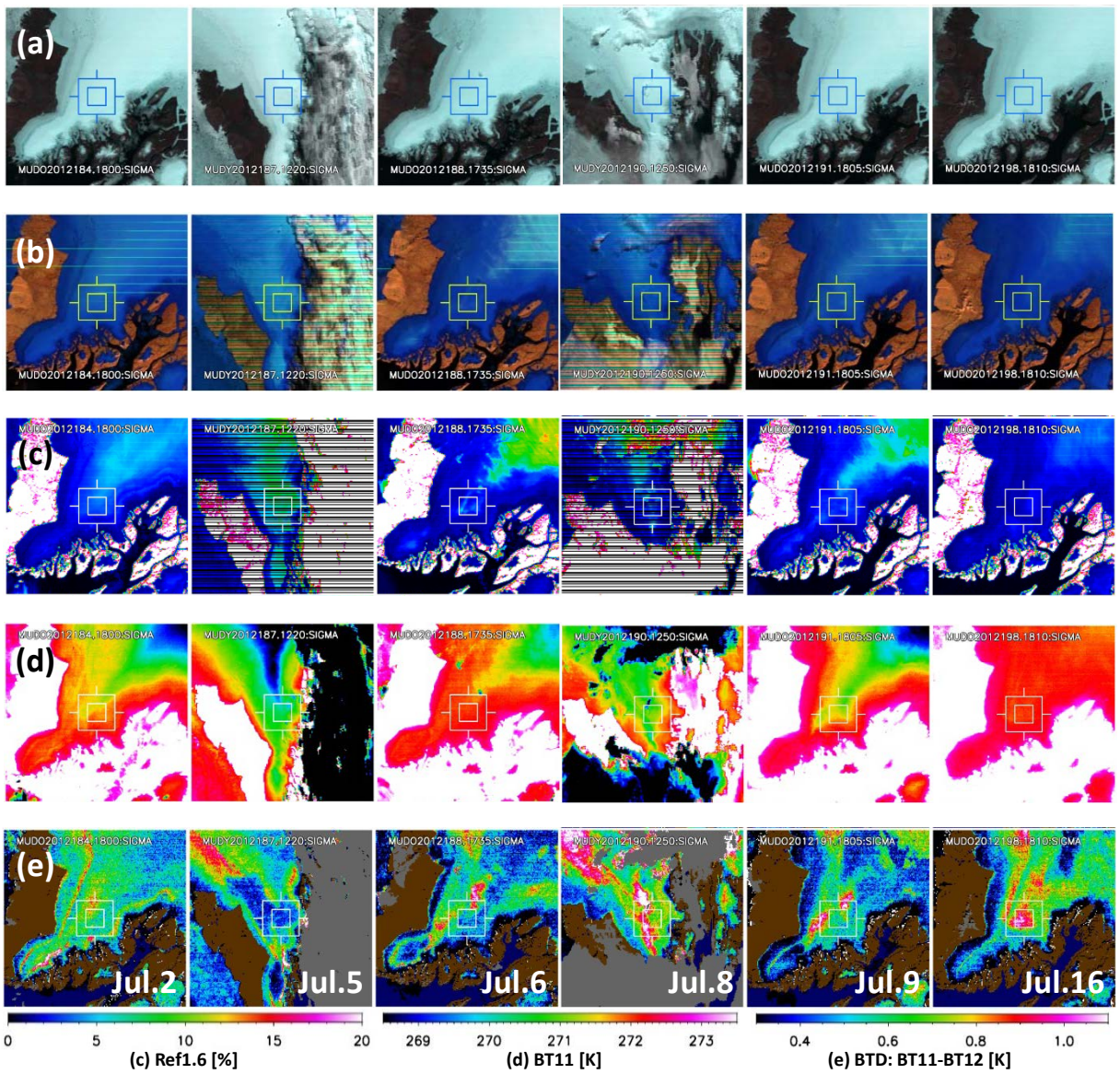

Fig. 4 Match-up analysis images of (a) MODIS true-color RGB composite, (b) false-color RGB composite, (c) reflectance at the wavelength (λ) of 1.6 μm ($Ref1.6_{sat}$), (d) brightness temperature at λ = 11 μm ($BT11_{sat}$), and (e) brightness temperature difference between MODIS channels 31 and 32 ($BTD_{sat} = BT11_{sat} - BT12_{sat}$) observed at the SIGMA-A site during the in situ observation period (2, 5, 6, 8, 9, and 16 July 2012). The SIGMA-A site is located at the center of these images within the box. Color legends for Fig. 4 (c), (d), and (e) are shown at the bottom. In Fig. 4 (e), gray, brown, and blue colors denote clouds, bare land, and open ocean, respectively.

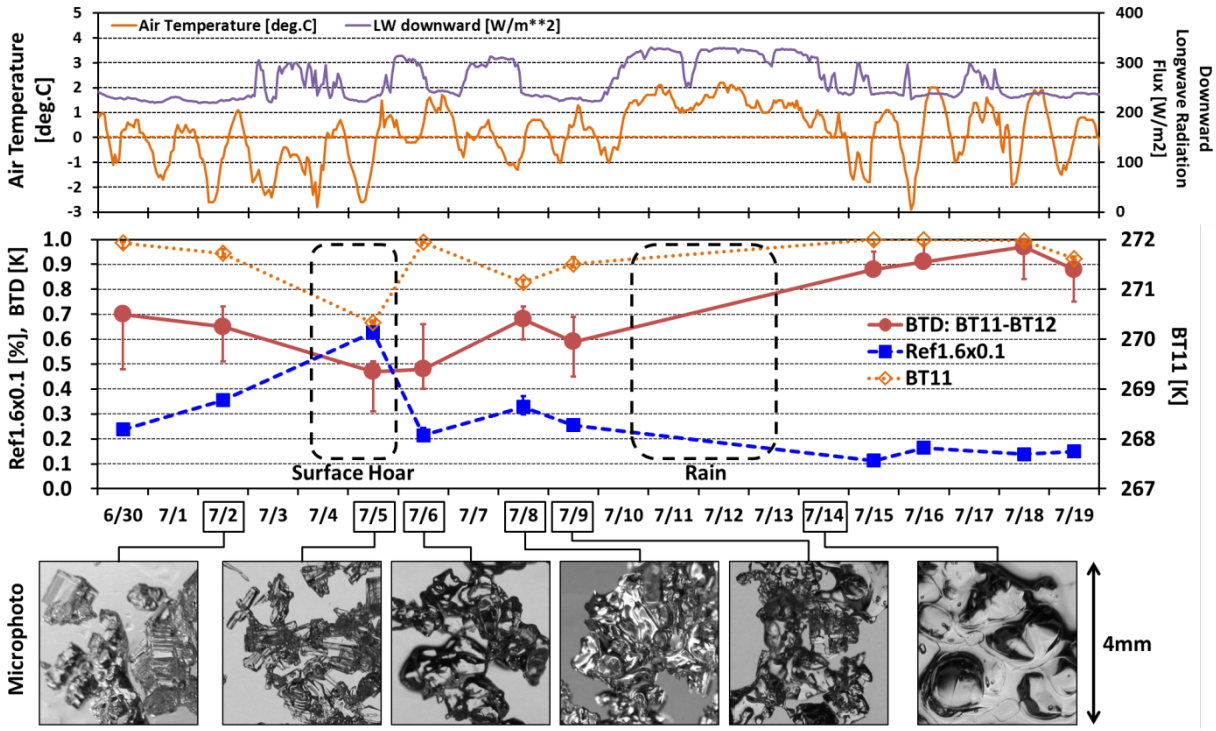

Fig. 5 (Upper) Temporal series of air temperature (°C) and downward longwave radiation flux (W/m^2) measured with the automatic weather station at the SIGMA-A site during 30 June to 19 July 2012. (Middle) Temporal variations of satellite-derived reflectance at λ = 1.6 μm ($Ref1.6_{sat}$ in %, the value of which is multiplied by 0.1), brightness temperature at λ = 11 μm ($BT11_{sat}$ in Kelvin), and brightness temperature difference between 11 μm and 12 μm (BTD_{sat} in Kelvin) extracted at the center pixel of the MUD images shown in Fig. 4. Error bars denote the maximum and minimum values within the surrounding eight pixels. (Lower) Micro-photos of surface snow crystals taken at the site.

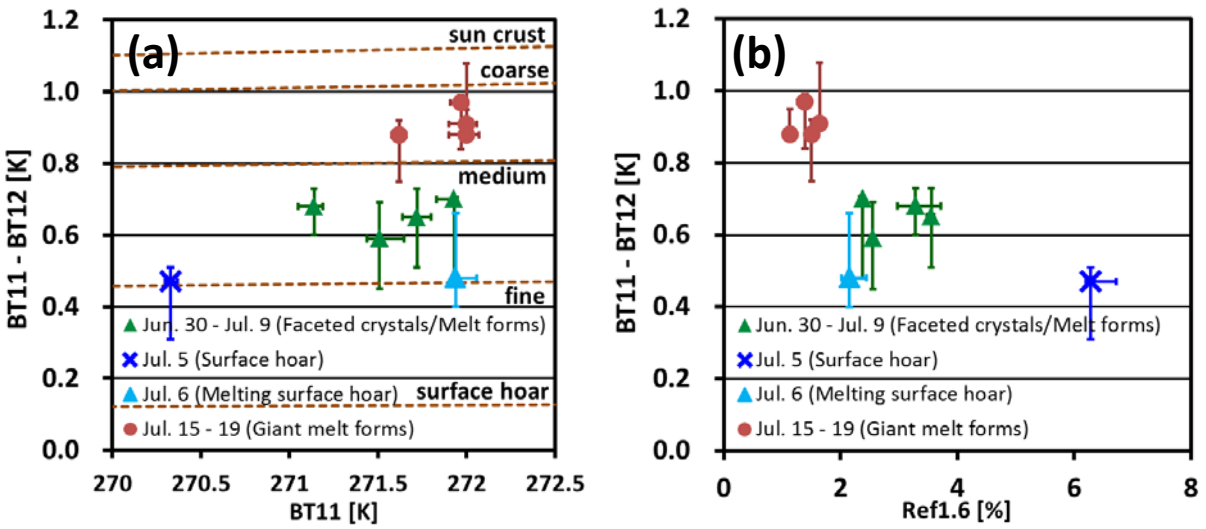

Fig. 6 Scatter plots of (a) Brightness temperature at λ = 11 μm ($BT11_{sat}$) and brightness temperature difference between 11 μm and 12 μm ($BTD_{sat} = BT11_{sat} - BT12_{sat}$) and (b) reflectance at λ = 1.6 μm ($Ref1.6_{sat}$) and BTD_{sat} extracted from the center pixel of the match-up image in Fig. 4. Error bars denote the maximum and minimum values within the surrounding eight pixels. Also plotted in the left figure are the expected BTD lines, which are averages of the simulated BTD_{sim} at near-nadir satellite zenith angles between 0 and 30° shown in Fig. 3.

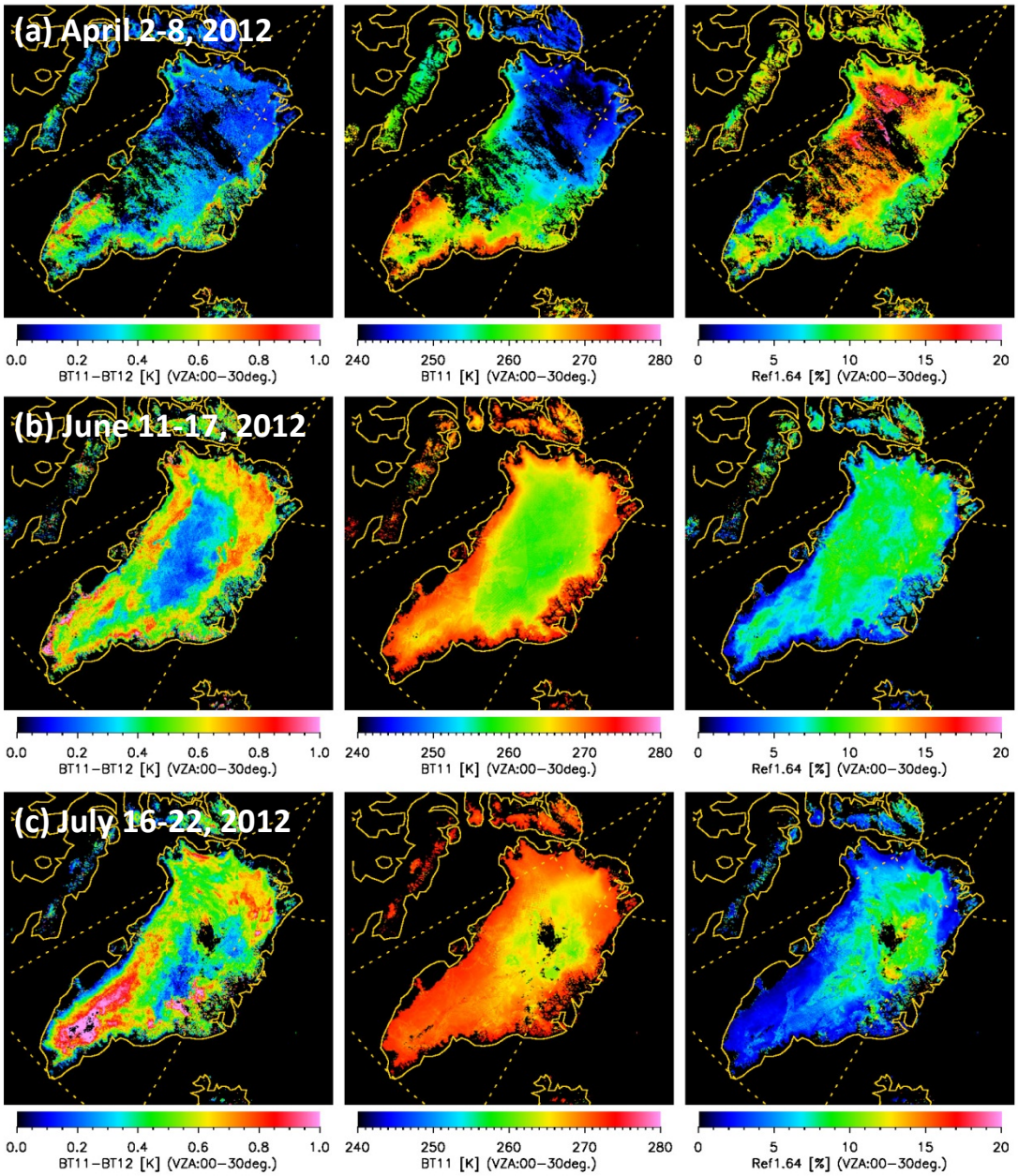

Fig. 7 Spatial distribution of brightness temperature difference (BTD_{sat}) between 11 μm and 12 μm (left), brightness temperature at λ = 11 μm ($BT11_{sat}$) (middle), and reflectance at λ = 1.6 μm ($Ref1.6_{sat}$) (right) observed over the Greenland ice sheet in the period of (a) 2–8 April, (b) 11–17 June, and (c) 16–22 July 2012. The black color over the ice sheet denotes remaining cloudy areas that could not be eliminated in the weekly composite period.

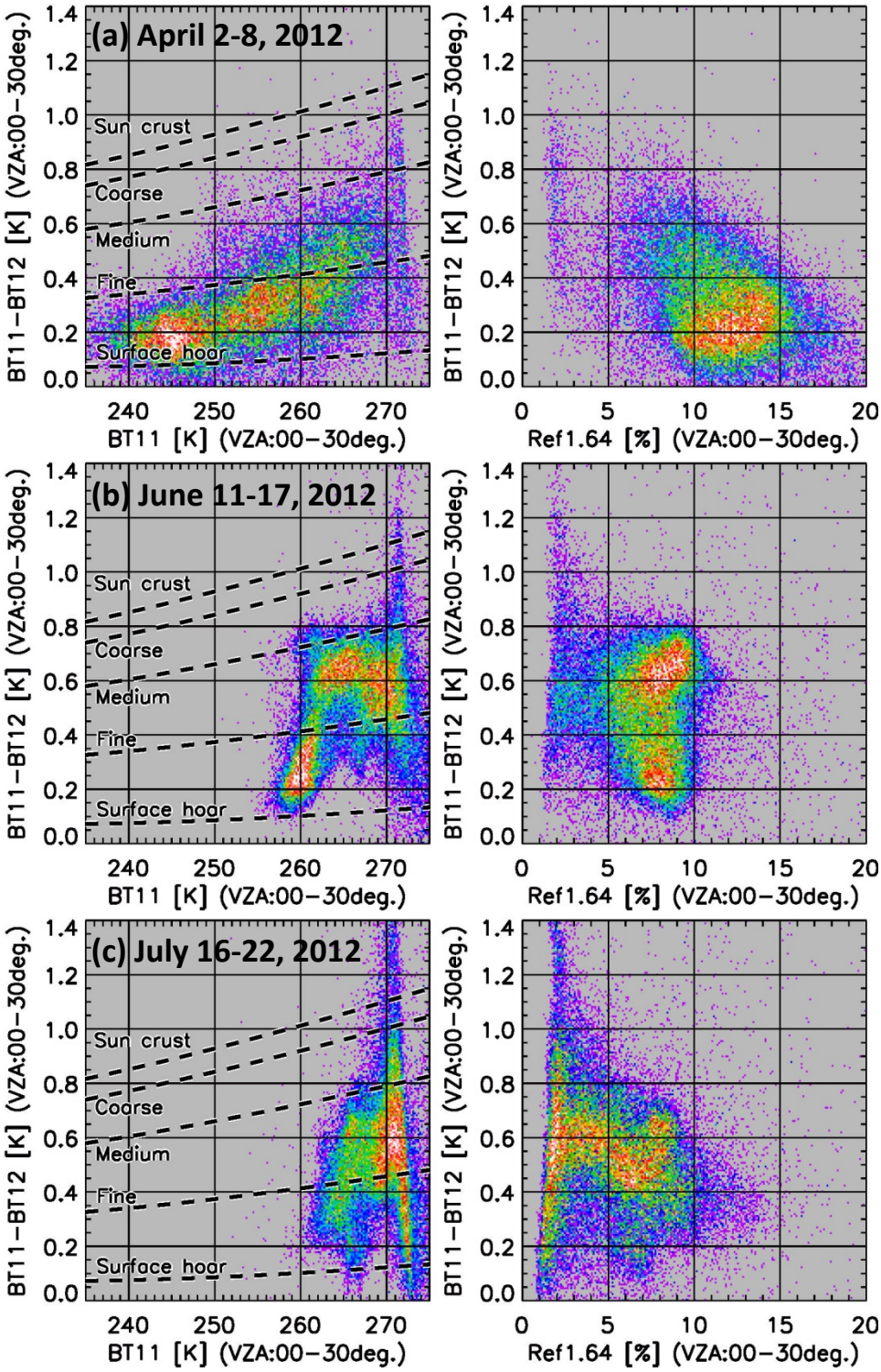

Fig. 8 Scatter plot between $BT11_{sat}$ and BTD_{sat} (left column) and $Ref1.6_{sat}$ and BTD_{sat} (right column) extracted from the images shown in Fig. 7 in the period of (a) 2–8 April, (b) 11–17 June, and (c) 16–22 July 2012. Also plotted in the left column figures are the expected BTD lines for the snow types of surface hoar, fine snow, medium melt forms, coarse melt forms, and sun crust, which are averages of the simulated BTD_{sim} at near-nadir satellite zenith angles between 0–30° shown in Fig. 3.